

See discussions, stats, and author profiles for this publication at: <https://www.researchgate.net/publication/225605819>

Selectivity Tailoring in Liquid Phase Oxidation Over MWNT-Mn₃O₄ Nanocomposite Catalysts

ARTICLE in THE JOURNAL OF PHYSICAL CHEMISTRY C · AUGUST 2011

Impact Factor: 4.77 · DOI: 10.1021/jp203318n

CITATIONS

11

READS

84

8 AUTHORS, INCLUDING:



Mandakini Biswal

CSIR - National Chemical Laboratory, Pune

8 PUBLICATIONS 157 CITATIONS

SEE PROFILE



Vivek Ramkrushna Mate

8 PUBLICATIONS 46 CITATIONS

SEE PROFILE



Pradip S Pachfule

CSIR - National Chemical Laboratory, Pune

44 PUBLICATIONS 1,017 CITATIONS

SEE PROFILE



Kanika L Agrawal

University of Michigan

5 PUBLICATIONS 13 CITATIONS

SEE PROFILE

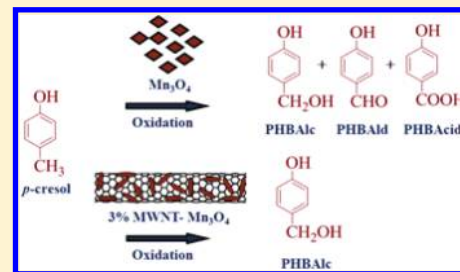
Selectivity Tailoring in Liquid Phase Oxidation Over MWNT-Mn₃O₄ Nanocomposite Catalysts

Mandakini Biswal,^{†,‡} Vivek V. Dhas,[†] Vivek R. Mate,[‡] Abhik Banerjee,[†] Pradip Pachfule,[†] Kanika L. Agrawal,[†] Satishchandra B. Ogale,^{*,†} and Chandrashekhar V. Rode^{*,‡}

[†]Physical and Material Chemistry Division and [‡]Chemical Engineering and Process Development Division, National Chemical Laboratory (CSIR), Pune, India

S Supporting Information

ABSTRACT: Highly selective multiwalled nanotubes (MWNT)-Mn₃O₄ nanocomposite catalyst was designed for liquid phase oxidation of *p*-cresol, which gave highest selectivity of 90% to the first step oxidation product, *p*-hydroxy benzyl alcohol. Mn₃O₄ nanoparticles and MWNT-Mn₃O₄ nanocomposites were synthesized by coprecipitation route using mixed precursors under controlled conditions. The phase purity of Mn₃O₄ and the formation of MWNT-Mn₃O₄ nanocomposites were confirmed by X-ray diffraction, Raman spectroscopy, and X-ray photoelectron spectroscopy. High-resolution transmission electron microscopy revealed the selective exposure of (101) and (001) planes of Mn₃O₄ nanoparticles in the MWNT-Mn₃O₄ composite, while lowering in oxidizing capacity of MWNT-Mn₃O₄ nanocomposite confirmed by cyclic voltametry was due to incorporation of electron rich MWNT. Thus, selectivity tuning of the new material (MWNT-Mn₃O₄ nanocomposite) was found to be due to alteration in both geometric as well as electronic properties. A plausible reaction pathway also has been proposed involving the predominant role of nucleophilic lattice oxygen (O²⁻) species due to exposure of particular crystal planes giving highest selectivity to *p*-hydroxy benzyl alcohol.



1. INTRODUCTION

Catalytic liquid phase oxidation of alkyl groups in substituted phenols is a core technology in fine chemicals and pharmaceutical industries.^{1–4} Therefore developing new materials by modifying their intrinsic properties has been a continuing effort for the last two decades.^{5–8} The major challenges in developing new catalysts are (i) stability of the metal function without leaching under oxidation conditions, (ii) maintaining activity in the presence of antioxidizing substrates like cresols, (iii) tailoring selectivity to the desired oxidation products, particularly to the first step oxidation product, and (iv) minimizing reaction time as well as the catalyst concentration. *p*-Cresol oxidation is an example of industrial oxidation process which involves step-wise oxidation to give a mixture of *p*-hydroxy benzyl alcohol, *p*-hydroxy benzaldehyde, and *p*-hydroxy benzoic acid depending upon the catalyst used and reaction conditions.^{5–7,9,10} Among these, both alcohol and aldehyde derivatives are important intermediates for the manufacture of vanillin (a widely used flavoring agent), trimethoxy benzaldehyde, various agrochemicals, and pharmaceuticals such as semisynthetic penicillin, amoxicillin, and the antiemetic drug trimethobenzamide.^{4,11,12} Efficient catalysts for oxidation reactions mainly involve oxides of transition metals having capability to form redox couples. In particular, Co-based catalysts systems and metals such as Cu, Mn supported on molecular sieves, carbon, or resins have been extensively studied for this oxidation reaction.^{13–16} Apart from this, γ -Fe₂O₃ has also been used as efficient catalyst, but it has

been used for the oxidation of first step oxidation product of *p*-cresol, that is, *p*-hydroxy benzyl alcohol.¹⁷ Among different types of catalysts, nanostructured catalysts showed higher activity than their bulk counterparts as shown in our work on nanostructured Co₃O₄ catalysts,¹⁸ which could not only be due to the size reduction (high surface/volume ratio) alone but also the modified adsorption characteristics caused by geometric and electronic effects. Hence this work was undertaken to further explore and understand the fundamental aspects of the nanostructured materials that govern their performance, especially their role in directing the selectivity pattern in a consecutive oxidation reaction. For this purpose, we have synthesized nanostructured Mn₃O₄ and its composites with multiwalled carbon nanotube (MWNT) in different degrees of loading and investigated the correlation between its constitution, structural aspects, and the activity for oxidation of *p*-cresol. Mn₃O₄ alone has been reported for catalytic oxidation of methane, carbon monoxide,¹⁹ decomposition of NO and N₂O,^{20–22} deoxygenation of nitrobenzene,²³ while MWNT-Mn₃O₄ nanocomposite has been studied for only supercapacitor and magnetism applications.^{24,25} To the best of our knowledge, ours is a first report of highly selective MWNT-Mn₃O₄ nanocomposite developed for selective liquid phase oxidation of *p*-cresol to intermediate *p*-hydroxy benzyl

Received: April 9, 2011

Revised: June 24, 2011

Published: July 05, 2011

alcohol under mild conditions. The selective formation of intermediate *p*-hydroxy benzyl alcohol in a sequential oxidation of *p*-cresol could be attributed to the alterations in geometric as well as electronic characteristics of Mn_3O_4 by introducing electron rich rigid material like MWNT. The role of both these aspects has been studied in detail by high-resolution transmission electron microscopy (HR-TEM), X-ray diffraction (XRD), X-ray photoelectron spectroscopy (XPS), Raman spectroscopy and cyclic voltametry (CV).

2. EXPERIMENTAL SECTION

2.1. Materials. Manganese acetate tetrahydrate, ethanol, and xylene were obtained from Merck. Oleylamine was taken from Fluka. *p*-Cresol was supplied by Loba Chemie, while sodium hydroxide was obtained from Merck. MWNT was purchased from Aldrich Chemicals. Analytical grade and HPLC grade methanol and *n*-propanol were obtained from Rankem.

2.2. Catalyst Preparation. Nanostructured Mn_3O_4 was prepared using manganese acetate, oleylamine, xylene, and ethanol by coprecipitation method.²⁶ In order to prepare 3% MWNT- Mn_3O_4 nanocomposite, commercially available MWNT was first functionalized with HNO_3 and H_2SO_4 in 1:3 ratio. In a typical procedure, 0.24 g of manganese acetate and 0.0075 g of functionalized MWNT were properly dispersed in xylene at room temperature for 30 min. To this, 4 mL of oleylamine was added and this mixture was then transferred to a round-bottom flask that was heated from room temperature to 363 K under stirring. After the temperature reached 363 K, 1 mL H_2O was added and the stirring was continued at this temperature for 3 h. Then the mixture was cooled to room temperature, and highly dispersed 3% MWNT- Mn_3O_4 nanocomposite was made to settle down by the addition of sufficient amount of ethanol. Then the solid material was isolated by centrifugation. The nanocomposite powder thus obtained was dried at 333 K for 3 h. The same procedure was followed for the synthesis of other MWNT- Mn_3O_4 composites with different degrees of loadings by varying the ratio of Mn_3O_4 to MWNT.

2.3. Characterization of Catalysts. The synthesized catalyst samples were characterized by X-ray powder diffraction using Philips X'Pert PRO diffractometer with nickel-filtered $\text{Cu K}\alpha$ radiation, Raman spectroscopy using LabRAM HR800 from JY Horiba, high-resolution transmission electron microscopy using IFEI, Tecnai F30, with 300 KV FEG and field-emission scanning electron microscopy (FESEM; Hitachi S-4200). The surfaces of the catalysts were examined by X-ray photoelectron spectroscopy on a VG scientific ESCA-3000 spectrometer using nonmonochromatized $\text{Mg K}\alpha$ radiation (1253.6 eV) at a pressure of about 1×10^{-9} Torr. The surface area values of all the samples were determined by Brunauer–Emmett–Teller (BET) adsorption method (Quadrascorb automatic volumetric instrument). The percentage metal oxide loading was calculated from ICP (inductive coupled plasma) analysis with Spectro 165 high-resolution ICP-OES Spectrometer (model no. ARCOSFHS12). All the cyclic voltametry measurements were done with Autolab PGSTAT30 (Eco-Chemie).

2.4. Catalytic Activity. All the catalytic oxidation reactions were carried out in a 300 cm^3 capacity high-pressure Hastelloy reactor supplied by Parr Instruments Co. U.S.A. The reactor was connected to an air reservoir held at a pressure higher than that of the reactor. A Hewlett-Packard model 1050 liquid chromatograph equipped with an ultraviolet detector was used for the

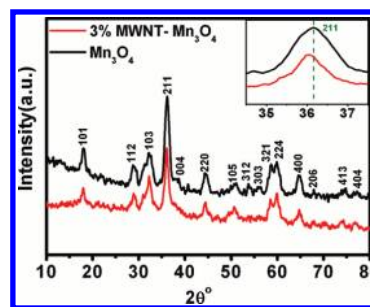


Figure 1. XRD spectra of Mn_3O_4 and 3% MWNT- Mn_3O_4 ; inset shows shift of (211) peak toward lower 2θ due to addition of MWNT.

analysis. HPLC analysis was performed on a 25 cm RP-18 column supplied by Hewlett-Packard. The products and reactants were detected using a UV detector at $\lambda_{\text{max}} = 223$ nm. Aqueous methanol (35%) was used as mobile phase at a column temperature of 308 K and a flow rate of 1 mL/min. Samples of 10 μL were injected into the column using an auto sampler HP 1100.

In a typical experiment, 3 g of *p*-cresol, 4.5 g of NaOH, and 70 cm^3 of *n*-propanol were heated in a flask with a reflux condenser until the NaOH dissolved completely. This reaction mixture was charged to a 300 cm^3 par autoclave. Then 0.02 g catalyst was added, and the reaction mixture was heated to 373 K. After the desired temperature was attained, the reactor was pressurized with 6.5 bar nitrogen and 2.4 bar oxygen. Then the reaction was started by agitating at 900 rpm. When the pressure decreased, the reactor was again filled by oxygen. This was continued up to 2 h. The progress of the reaction was monitored by observing the pressure drop in the reservoir vessel as a function of time. After 2 h the reactor was cooled to room temperature and the unabsorbed nitrogen gas was vented out. Then the content of the reactor was discharged and the final volume was noted down. The final samples were analyzed by HPLC.

3. RESULTS AND DISCUSSION

3.1. Catalyst Characterization. As shown in Figure 1, the XRD patterns of both Mn_3O_4 and 3% MWNT- Mn_3O_4 nanocomposites were identical with an intense peak at $2\theta = 36^\circ$ corresponding to (211) plane. The other peaks of lower intensity were also identical for both the samples and matched with those of tetragonal hausmannite phase (JCPDS card no. 24-0734). In both samples, no other peaks corresponding to any impurity phase(s) were seen, confirming that the product was tetragonal Mn_3O_4 . In order to distinguish Mn_3O_4 from $\gamma\text{-Mn}_2\text{O}_3$, which has similar structure and unit cell parameter as that of Mn_3O_4 ,²⁷ our samples were also characterized by other techniques, which are discussed below. No signature of MWNT was observed in the XRD spectra of MWNT- Mn_3O_4 nanocomposite due to low concentration (only a few percent) of MWNT in the composite. Also there is a considerable shift in the peaks of MWNT- Mn_3O_4 composites toward lower 2θ value as shown in the inset of Figure 1. This shift in the peak is due to the strain involved during the formation of nanocomposites.

The Raman spectra for Mn_3O_4 , MWNT, and MWNT- Mn_3O_4 nanocomposite are shown in Figure 2. A single intense peak at 659 cm^{-1} confirmed the highly pure phase of the synthesized Mn_3O_4 .²⁸ In the case of the MWNT sample, the two peaks

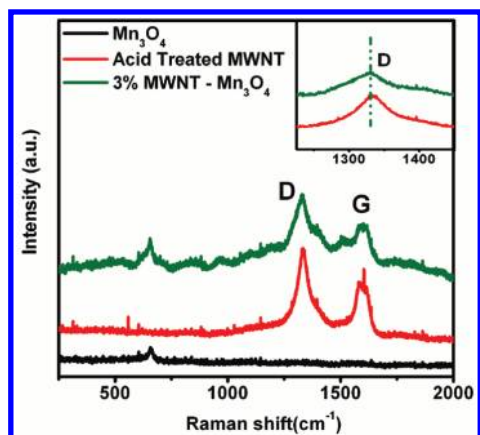


Figure 2. Raman spectra of Mn_3O_4 , acid treated MWNT, 3% MWNT- Mn_3O_4 ; inset shows broadening of D band.

observed at 1328 and 1579 cm^{-1} correspond to D and G bands, respectively, which match well with those reported in the literature.²⁹ In the case of 3% MWNT- Mn_3O_4 nanocomposite sample, distinct peaks corresponding to MWNTs as well as Mn_3O_4 are observed. The interesting feature of the Raman spectra of MWNT- Mn_3O_4 nanocomposite is the broadening of the Mn_3O_4 and MWNT peaks as compared to the bare Mn_3O_4 nanoparticles and MWNT case. The broadening of D band of MWNT is shown in the inset of Figure 2. Such a broadening can occur because of two possibilities viz. (i) strain gradient originating from interface integration during the formation of MWNT- Mn_3O_4 composite, which involves anchoring of Mn_3O_4 on the molecular moiety like $-\text{COOH}$ due to functionalization of MWNT and/or (ii) slightly broader particle size distribution, which in the present case was in the range of 12–15 nm. This increase in particle size can also be correlated with the inset figure in XRD spectra which was shown in Figure 1, where the peak is slightly broader in the case of Mn_3O_4 than 3% MWNT- Mn_3O_4 nanocomposite. In addition, the nanosized nature of the material leads to a higher concentration of surface atoms and attendant phonon softening that can contribute to peak broadening. Such broadening is also reported in the case of TiO_2 -MWNT nanocomposite.³⁰

X-ray photoelectron spectroscopy was used to determine the surface oxidation states of all the species present in the bare Mn_3O_4 nanoparticles and various percentages of nanocomposites (Figure 3a–f). Figure 3a,b show the C1s XPS spectra of pristine MWNT and acid-functionalized MWNT, respectively. Please note the different energy (x -axis) scales on the two figures. In the case of pristine MWNT, the C1s peak can be resolved into two peaks that represent presence of two distinct chemical states of carbon on the surface of MWNT. The peak at the binding energy 284.6 eV corresponds to C–C carbon,³¹ and the peak at 286.1 eV is due to C–O carbon. Upon acid functionalization of MWNT, the C1s peak structure is seen to be modified significantly. After deconvolution, it exhibits four contributions for the best fit. The most resolved peak located at 284.6 eV is once again assigned to the C–C bonds, while the other three peaks having binding energies of 285.4, 286.9, and 290.1 eV correspond to carbon in the C–O, carbonyl (C=O), and carboxyl ($-\text{COOH}$) bonds, respectively.^{24,32,33} Emergence of the new contributions clearly signifies introduction of polar oxygen groups into the surface of MWNT.

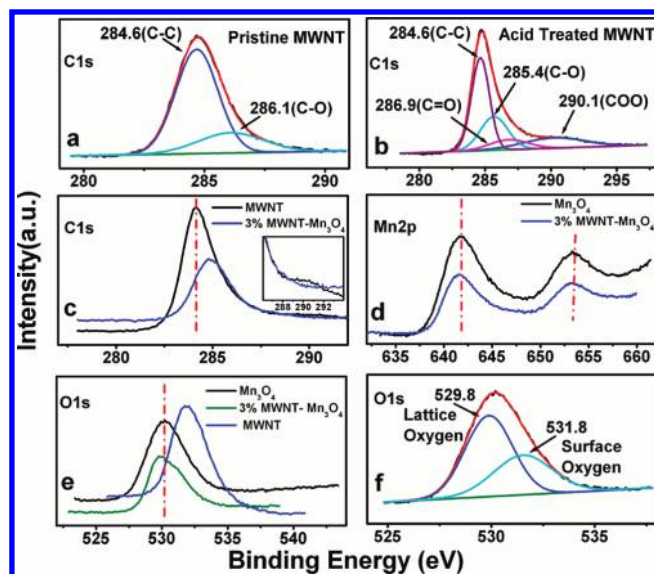


Figure 3. XPS spectra of (a) C1s spectra of pristine MWNT, (b) C1s spectra of acid treated MWNT, (c) comparison of C1s spectra of MWNT, 3% MWNT- Mn_3O_4 . Inset shows the enlarged view of the 285 to 295 eV binding energy region. (d) comparison of Mn2p spectra for Mn_3O_4 , 3% MWNT- Mn_3O_4 , (e) comparison of O1s XPS spectra Mn_3O_4 , 3% MWNT- Mn_3O_4 , MWNT, and (f) O1s spectra of 3% MWNT- Mn_3O_4 .

The C1s spectra of MWNT- Mn_3O_4 nanocomposite (3% case shown, others at low concentrations being nominally similar) and MWNT nanoparticles are compared in Figure 3c, which reveals a significant shift toward the higher binding energy in the case of the nanocomposites. This shift can be attributed to the considerable strain imparted to the C–C bond configuration of MWNT and the related modification of the electronic environment due to the anchoring of Mn_3O_4 nanoparticles on the surface of MWNT. The inset to Figure 3c is the enlarged view of the same spectra in the region of the binding energy from 285 to 295 eV. A distinct hump is clearly seen around 290 eV in the spectrum of MWNT that is due to the carboxylic group on the surface of MWNT. But this hump is absent in the case of the nanocomposite. This signifies the attachment of Mn_3O_4 to the carboxylic oxygen present on the surface of MWNT.

Figure 3d shows the comparison of the Mn2p XPS spectra for 3% MWNT- Mn_3O_4 nanocomposite and bare Mn_3O_4 nanoparticles. These two spectra are nearly similar having almost equal binding energy. The peak at a binding energy of 641.7 eV is due to $\text{Mn}2\text{p}_{3/2}$ and the peak at 653.3 eV is assigned to $\text{Mn}2\text{p}_{1/2}$. These binding energy values match with the reported values for Mn_3O_4 .^{24,34–36}

The comparison of O1s spectra for MWNT, bare Mn_3O_4 , and 3% MWNT- Mn_3O_4 are shown in Figure 3e. Comparing all the O1s spectra, it can be seen that there is a shift in the case of the nanocomposites toward lower binding energy, which is again due to the strain involved during the formation of composites. The O1s peaks for the nanocomposites are more similar to the O1s peak of bare Mn_3O_4 , which is due to the uniform dispersion of Mn_3O_4 nanoparticles on the surface of MWNT with good surface coverage. The binding energy for O1s is shown in Figure 3f for the case of 3% MWNT- Mn_3O_4 . After deconvolution, the peak shows two contributions. The peak at a binding energy of 529.8 eV is due to the lattice oxygen and the peak present at 531.8 eV can be attributed to either surface OH groups or other oxygen containing groups.³⁴

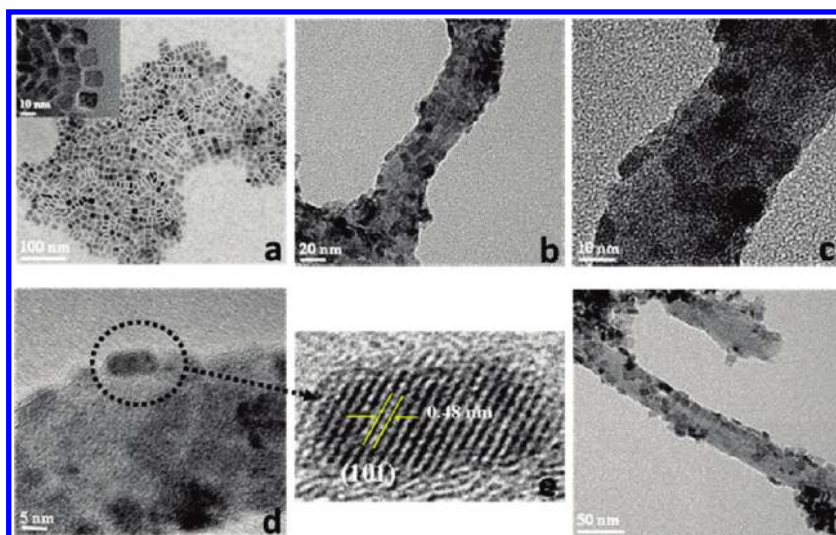


Figure 4. (a) HR-TEM image of Mn_3O_4 ; inset is a high-magnification image showing 8–10 nm particles. (b–f) HR-TEM image of 3% MWNT- Mn_3O_4 .

Table 1. BET Surface Area Measurements of Mn_3O_4 , MWNT, 3% MWNT- Mn_3O_4

Sl. no	catalyst	BET surface area (m^2/g)
1	Mn_3O_4	65.89
2	3% MWNT- Mn_3O_4	20.14
3	MWNT	15.5

Figure 4a shows HR-TEM image of Mn_3O_4 , revealing highly faceted morphology with a nanoparticle size in the range of 8–10 nm (Figure 4a inset). As shown in Figure 4b–f, MWNT- Mn_3O_4 nanocomposite is again faceted type but with some degree of elongation along the MWNT length. This could be attributed to the anisotropic surface diffusion of adsorbed species and the differential role of axis vs curvature. These nanoparticles are seen to be uniformly dispersed on the MWNT surface with a size distribution of ~ 12 – 15 nm (Figure 4c,d). Figure 4e is a section of a Mn_3O_4 nanoparticle showing the axial growth in the direction of (101) with a lattice spacing of 0.48 nm and the other exposed side along the (001) plane. This was inferred from the interplane angle measured directly from the HR-TEM image. All these HR-TEM images of MWNT- Mn_3O_4 composites indicate that most of the exposed sides of Mn_3O_4 nanoparticles were along two specific planes (101) and (001).

Table 1 shows the surface area values for bare Mn_3O_4 and the MWNT- Mn_3O_4 nanocomposites. The surface area of the bare Mn_3O_4 nanoparticles was found to be $65.8 \text{ m}^2/\text{g}$, which is seen to decrease substantially (to about $20 \text{ m}^2/\text{g}$) in the case of the 3% MWNT- Mn_3O_4 nanocomposite. This decrease in the surface area of nanocomposites could be due to the dispersion of Mn_3O_4 on a confined area of the MWNT matrix. This is also in accordance with the increase in particle size from 8–10 nm to 12–15 nm of bare Mn_3O_4 and MWNT- Mn_3O_4 nanocomposites, respectively. The surface area of only MWNT was found to be $15 \text{ m}^2/\text{g}$. In the nanocomposite, the Mn_3O_4 nanoparticles are anchored uniformly on the surface of MWNT, shielding some portion of the MWNT surface and dominating the m^2/g area estimate, albeit with somewhat enhanced size (12–15 nm).

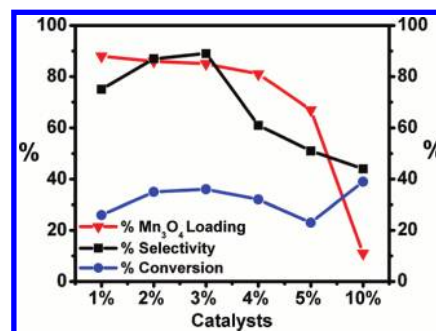


Figure 5. Percentage loading of Mn_3O_4 from ICP analysis in comparison with selectivity and conversion.

The percent loading of metal oxide in the composites was studied by ICP analysis. The highest metal loading of 88% was observed for the case of 1% MWNT- Mn_3O_4 catalyst (Figure 5). The percent loading slightly decreased from 88 to 86 and 85% for 2 and 3% MWNT cases, respectively. Beyond 3% MWNT case, the metal oxide loading decreased continuously and significantly to 11% in the case of 10% MWNT, the maximum MWNT concentration examined in this work. The percent conversion and the selectivity patterns roughly follow similar trend as a function of nanocomposite composition, except for the 10% case. Also they bear an interesting nonmonotonic correlation, vis a vis, the metal oxide loading. The % selectivity is seen to increase up to 90% in the case of 3% MWNT- Mn_3O_4 and then decreases. This could be explained by the relative degree of heterogeneous and homogeneous nucleation of Mn_3O_4 nanoparticles. At low MWNT concentration (e.g., the 1% MWNT- Mn_3O_4 case), due to less concentration of MWNT it is possible that a fraction of Mn_3O_4 nanoparticles is formed by homogeneous nucleation and the same is not anchored on MWNT leading to higher performance. With increasing percent of MWNT to 2 and 3%, more Mn_3O_4 nanoparticles would form on the surface of MWNT and homogeneous nucleation contribution should decrease (Figure 6) leading to increasing conversion and selectivity. For further increase in MWNT percent (e.g., 4–10%), although all

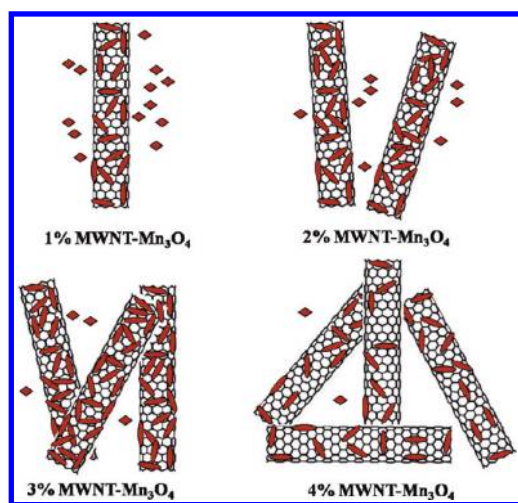
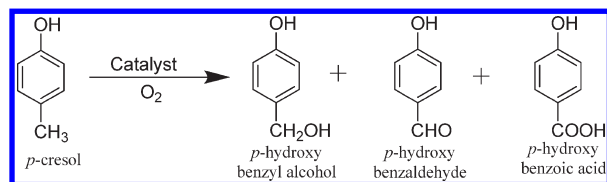


Figure 6. Possible homogeneous and heterogeneous nucleation of Mn_3O_4 nanoparticles in 1–4% MWNT- Mn_3O_4 nanocomposites.

Scheme 1. Reaction of *p*-Cresol



the nanoparticles would form on the MWNT surface, the exposed MWNT surface containing acid groups would get exposed more and more, leading to the formation of nonoxidation products. This would then decrease the selectivity considerably, as observed.

3.2. Activity Measurement. The activity results of bare Mn_3O_4 and MWNT- Mn_3O_4 nanocomposites for the oxidation of *p*-cresol are discussed on the basis of conversion of *p*-cresol and selectivity to various products. The % conversion and selectivity were calculated by using eqs 1 and 2 respectively as follows

$$\% \text{Conversion} = \frac{C_i - C_f}{C_i} \times 100 \quad (1)$$

$$\% \text{Selectivity} = \frac{C_p}{C_x} \times 100 \quad (2)$$

where

C_i = initial concentration of *p*-cresol

C_f = final concentration of *p*-cresol

C_p = concentration of product formed

C_x = concentration of *p*-cresol consumed

In order to study the product distribution, a few preliminary experiments of *p*-cresol oxidation were carried out using Mn_3O_4 and MWNT- Mn_3O_4 nanocomposites in *n*-propanol solvent under high-pressure conditions. The progress of the reaction was monitored by liquid phase analysis as a function of time. It was observed that the initial oxidation product was *p*-hydroxy benzyl alcohol that undergoes further oxidation to give *p*-hydroxy benzaldehyde and *p*-hydroxy benzoic acid. On the basis of

this the reaction pathway of *p*-cresol oxidation is shown in Scheme 1.

Results on catalyst screening for *p*-cresol oxidation are shown in Figure 7. Bare Mn_3O_4 shows 46% conversion of *p*-cresol and a selectivity of 43% toward *p*-hydroxy benzyl alcohol, the remaining constituents being *p*-hydroxy benzaldehyde and *p*-hydroxy benzoic acid. *p*-cresol conversion decreased to 26 and 35% in the case of 1 and 2% MWNT- Mn_3O_4 nanocomposites. In the case of 3% MWNT- Mn_3O_4 , the conversion remains almost same, that is, 36%. But conversion decreases in the case of 4 and 5%, which was 32 and 23%, respectively. This decrease in *p*-cresol conversion for MWNT- Mn_3O_4 composite was not in the proportion to the decrease in surface area from 65 to 20 m^2/g for the change in material from bare Mn_3O_4 to MWNT- Mn_3O_4 composite respectively. Nevertheless, the decrease in surface area was attributed to the dispersion of Mn_3O_4 on a confined area of MWNT that also might restrict the access of substrate molecules to the active sites on the surface of catalyst. This explanation is supported by a separate oxidation experiment carried out using a physical mixture of 3% MWNT and Mn_3O_4 in which 42% conversion of *p*-cresol was obtained which was very close to that obtained for bare Mn_3O_4 . This experiment also showed that the selectivity of *p*-hydroxy benzyl alcohol is due to the composite formation only.

It is interesting to note a steep increase in the selectivity to an intermediate product, *p*-hydroxy benzyl alcohol up to 90% for both 2 and 3% MWNT- Mn_3O_4 composite catalysts as compared to 43% in the case of bare Mn_3O_4 . *p*-Cresol oxidation over a variety of heterogeneous catalysts reported so far (Supporting Information, Table 1), has shown mainly the formation of *p*-hydroxy benzaldehyde. Thus, the challenging task of obtaining the highest selectivity up to 90% toward first step oxidation product (*p*-hydroxy benzyl alcohol) was achieved by 3% MWNT- Mn_3O_4 nanocomposites. The critical role of addition of MWNT on the selectivity pattern is discussed in detail below.

In the case of the MWNT- Mn_3O_4 nanocomposites, selective exposure of two planes (101) and (001) of Mn_3O_4 was observed due to the structured support unlike the case of bare Mn_3O_4 where several planes can be exposed to the substrate molecules. Such correlations between the exposure of selective planes and catalytic activity have been reported.^{37,38} Figure 8a represents the crystal structure of Mn_3O_4 , which corresponds to a normal spinel structure with Mn^{2+} and Mn^{3+} in tetrahedral and octahedral sites, respectively. The selectively exposed planes (001) and (101) appear as shown in Figure 8b,c, respectively, which clearly indicate that the (001) plane contains only Mn^{3+} species and the (101) is composed of a mixture of Mn^{3+} and Mn^{2+} species. Between Mn^{3+} and Mn^{2+} species, Mn^{3+} is active for oxidation of *p*-cresol, because of its ability to be reduced to Mn^{2+} thus forming a redox couple ($\text{Mn}^{3+} \leftrightarrow \text{Mn}^{2+}$). A plausible mechanistic pathway for *p*-cresol oxidation over MWNT- Mn_3O_4 composite is shown in Figure 9. This oxidation pathway is proposed considering the role of lattice oxygen as a primary oxidant in the oxidation process.^{23,39–41} As shown in Figure 9, the first step involves the adsorption of *p*-cresol molecule on the Mn^{3+} sites followed by C–H bond polarization.⁴² Formation of C–O bond takes place by the abstraction of one of the lattice oxygen associated with Mn^{3+} , which in turn gets reduced to Mn^{2+} as shown in the second step. The lattice oxygen vacancy created on the Mn^{3+} site is compensated by the neighboring Mn^{2+} atom. Concurrently, the electron produced at the Mn^{3+} center is transferred to the neighboring Mn^{2+} site. The molecular oxygen

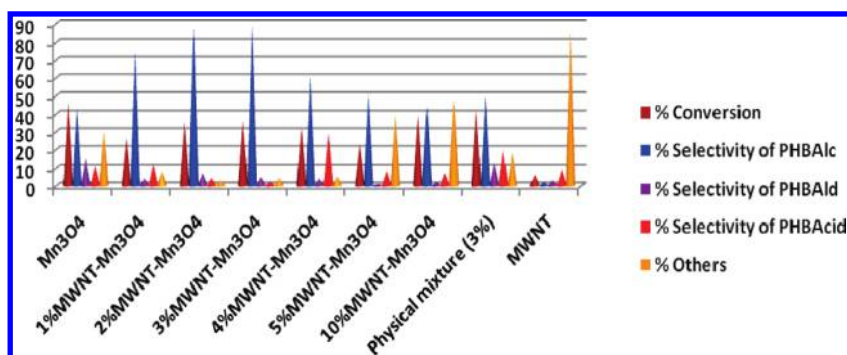


Figure 7. Activity results of the catalysts.

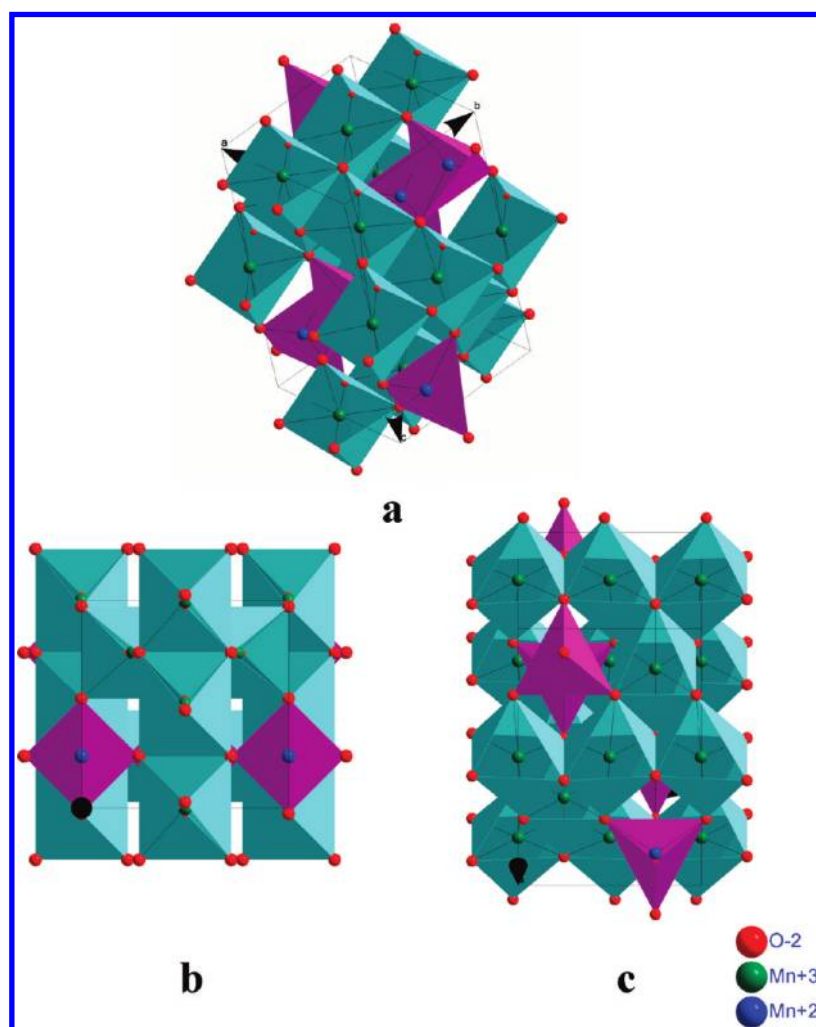


Figure 8. Crystal structure of (a) normal spinel Mn_3O_4 , (b) (001) plane of Mn_3O_4 spinel showing only Mn^{3+} , and (c) (101) plane of Mn_3O_4 showing both Mn^{2+} and Mn^{3+} .

is adsorbed on the vacant Mn^{2+} site and it gets converted to lattice oxygen to replenish the oxygen loss.⁴³ The last step involves desorption of *p*-hydroxy benzyl alcohol leading to the regeneration of catalyst, and another *p*-cresol molecule gets adsorbed and the cycle is repeated. Thus, Mn^{2+} and Mn^{3+} maintain a catalytic redox cycle for the conversion of molecular oxygen to lattice oxygen (O^{2-}) and hence the reoxidation of active centers (Mn^{3+}) takes place. Apart from the nucleophilic

lattice oxygen species O^{2-} , some other reactive electrophilic oxygen species such as O^- and O_2^- are also formed from the molecular oxygen.⁴³ However, it is considered that the formation of nucleophilic lattice oxygen species on the surface are responsible for selective oxidation, while the electrophilic oxygen species are considered as strong oxidants leading to deep oxidation products. In the case of the MWNT- Mn_3O_4 nanocomposite, the formation of lattice oxygen species may be

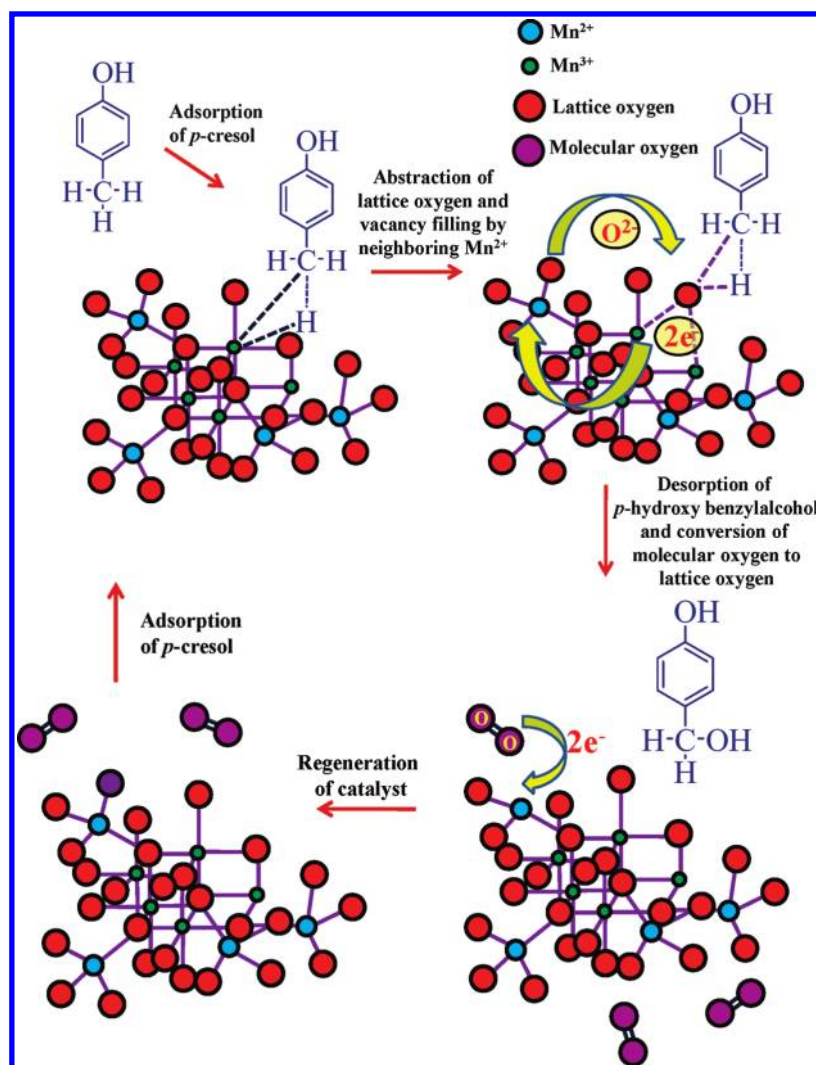


Figure 9. Possible mechanism pathway of oxidation of *p*-cresol to *p*-hydroxy benzyl alcohol.

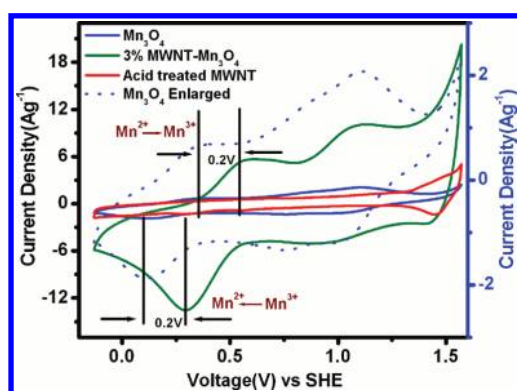


Figure 10. Cyclic voltammetry measurements of acid treated MWNT, Mn_3O_4 , and 3% MWNT- Mn_3O_4 .

more favored than the formation of electrophilic oxygen species due to the selective exposure of planes. This would lead to the oxidation of *p*-cresol primarily to *p*-hydroxy benzyl alcohol preventing the formation of subsequent oxidation products such as *p*-hydroxy benzaldehyde and *p*-hydroxy benzoic acid.

The selective formation of intermediate *p*-hydroxy benzyl alcohol can be also explained by comparing redox potential profiles of various catalysts obtained by CV measurements. For this purpose, CV measurements were performed at a scan rate of 50 mV s^{-1} for the acid-treated MWNT, Mn_3O_4 nanoparticles, and 3% MWNT- Mn_3O_4 nanocomposite samples over the potential range of 1.6 to -0.2 V with standard hydrogen electrode (SHE) and 2 M aqueous KCl solution. Figure 10 shows the plots of current density versus potential for all the above cases. Since MWNT did not show any oxidation activity (Figure 7) as expected, no oxidation or reduction peaks were observed. However, Mn_3O_4 nanoparticles and 3% MWNT- Mn_3O_4 nanocomposite showed clearly the presence of oxidation and reduction peaks (blue and green respectively, Figure 10). In both cases, the first anodic peak in the low potential region could be assigned to the oxidation of Mn^{2+} to Mn^{3+} , while the second one to the oxidation of Mn^{3+} to Mn^{4+} . Similarly, the cathodic peak present at higher potential could be assigned to the reduction of Mn^{4+} to Mn^{3+} and the second one to the reduction of Mn^{3+} to Mn^{2+} . Comparison of the reduction peaks of Mn_3O_4 nanoparticles and 3% MWNT- Mn_3O_4 nanocomposite, showed a clear and substantial shift ($\sim 200 \text{ mV}$) toward higher potential values for 3% MWNT- Mn_3O_4 nanocomposite. Reduction peak indicates the

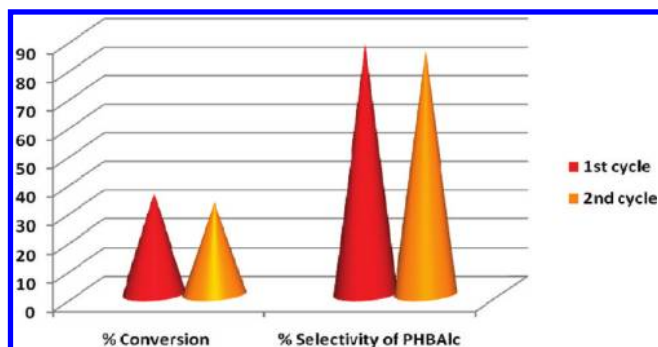


Figure 11. Catalyst recycling results of 3% MWNT-Mn₃O₄.

oxygen reduction ability hence, higher the potential value higher is the oxygen reduction ability, that is, lesser oxidizing ability. Thus lesser oxidizing ability of 3% MWNT-Mn₃O₄ composite than that of Mn₃O₄ is quite evident from their CV profiles. Similar study has been reported in the case of iron nitride-doped carbon nanofibers.⁴⁴ From this discussion, it can be inferred that Mn₃O₄ nanoparticles show higher oxidizing ability than that of MWNT-Mn₃O₄ nanocomposite, which results into deep oxidation giving a mixture of all the sequential oxidation products. Therefore, an electron rich system such as MWNT was deliberately introduced in the present composite to increase the electron density on Mn₃O₄ that restricts the oxidizing ability of the MWNT-Mn₃O₄ nanocomposite to achieve highest selectivity to *p*-hydroxy benzyl alcohol.

The selective formation of *p*-hydroxy benzyl alcohol (90%) could also be well correlated with the experimental observation that the moles of oxygen consumed for the *p*-cresol oxidation over MWNT-Mn₃O₄ nanocomposites are lower (0.026 mols) than those consumed over bare Mn₃O₄ (0.034 mols for 43% selectivity to alcohol and remaining aldehyde and acid) under identical conditions. With an increase in MWNT concentration from 4 to 10%, not only the selectivity to *p*-hydroxy benzyl alcohol is seen to decrease but also no other sequential oxidation product formation such as aldehyde and acid is noted. Instead other byproduct formation is observed. Similar product distribution was also observed for the case of only acid-treated MWNT where mainly other byproduct formation was observed without any significant conversion to well-defined sequential oxidation products. The decrease in selectivity in the case of 4, 5, and 10% MWNT nanocomposites can thus be attributed to the decrease in the percentage of Mn₃O₄ loading.

In order to study the stability of our catalysts, the recycling experiments were carried out in the following way: after the first oxidation run with the fresh 3% MWNT-Mn₃O₄ nanocomposite catalyst, it was filtered out and dried in an oven at 373 K for 3 h and was recharged to the reactor for the subsequent run. The procedure was followed for two subsequent oxidation experiments, and the results are shown in Figure 11. The catalyst was found to retain its activity even after second recycle. Also no leached component of the catalyst was found in the solution under the reaction conditions which is confirmed by its characterization.

4. CONCLUSION

The nanocomposites of Mn₃O₄ nanoparticles with functionalized MWNT (% MWNT between 0–10%) synthesized by coprecipitation route show excellent activity for liquid phase

oxidation of *p*-cresol. It was clear from CV analysis that introduction of an electron rich system such as MWNT increased the electron density over Mn₃O₄ that could control the deep oxidation ability resulting in highest selectivity toward the first step oxidation product, that is, *p*-hydroxy benzyl alcohol. Also HR-TEM results reveal the exposure of particular crystal planes (101, 001) of Mn₃O₄ in the case of the nanocomposite that favors the formation of nucleophilic lattice oxygen (O²⁻) species responsible for the highest selectivity of 90% to *p*-hydroxy benzyl alcohol, which was dramatically higher than that observed for the bare Mn₃O₄ nanoparticles (43%). The catalyst was recycled twice with retention of its activity. No leached components of the catalyst were found in solution under the reaction conditions of the present work.

■ ASSOCIATED CONTENT

S Supporting Information. A summary of literature on various heterogeneous catalyst systems used for oxidation of *p*-cresol has been given as Table 1 in the Supporting Information. This material is available free of charge via the Internet at <http://pubs.acs.org>.

■ AUTHOR INFORMATION

Corresponding Author

*Tel: +91-20-2590 2349. Fax: +91-20-2590-2621. E-mail address: (C.V.R.) cv.rode@ncl.res.in; (S.B.O.) satishogale@gmail.com.

■ ACKNOWLEDGMENT

The authors gratefully acknowledge Council of Scientific and Industrial Research (CSIR) for providing funding for this work. The authors would also like to thank Dr. Nandini Devi for her help in the crystal models. Also, we would like to thank Dr. Sreekumar and Sreekuttan for CV measurements.

■ REFERENCES

- (1) Sittig, M. *Chemical Technology Review: Pharmaceutical Manufacturing Encyclopedia*; Noyes Data Corporation: Park Ridge, NJ, 1997.
- (2) Clonts, K. E.; McKetta, R. A. *Kirk-Othmer Encyclopedia of Chemical Technology*, 3rd ed.; Wiley-InterScience: New York, 1978.
- (3) Burdock, G. A. *Encyclopedia of Food and Color Additives*; CRC Press: New York, 1997.
- (4) Torii, S.; Tanaka, H.; Siroi, T.; Akada, M. *J. Org. Chem.* **1979**, *44*, 3305.
- (5) Kshirsagar, V. S.; Garade, A. C.; Patil, K. R.; Jha, R. K.; Rode, C. V. *Ind. Eng. Chem. Res.* **2009**, *48*, 9423.
- (6) Rode, C. V.; Sonar, M. V.; Nadgeri, J. M.; Chaudhari, R. V. *Org. Proc. Res. Dev.* **2004**, *8*, 873.
- (7) Milone, C.; Ingoglia, R.; Neri, G.; Pistone, A.; Galvagno, S. *Appl. Catal. A* **2001**, *211*, 251.
- (8) Sharma, S. N.; Chandalia, S. B. *J. Chem. Technol. Biotechnol.* **1990**, *49*, 141.
- (9) Rode, C. V.; Kshirsagar, V. S.; Nadgeri, J. M.; Patil, K. R. *Ind. Eng. Chem. Res.* **2007**, *46*, 8413.
- (10) Kshirsagar, V. S.; Garade, A. C.; Patil, K. R.; Shirai, M.; Rode, C. V. *Top Catal* **2009**, *52*, 784.
- (11) Poss, A. J.; Belter, R. K. *J. Org. Chem.* **1988**, *53*, 1535.
- (12) Rao, D. V.; Stuber, F. A. *Synthesis* **1983**, *4*, 308.
- (13) Yumin, L.; Sheitian, L.; Kaizheng, Z.; Xingkai, Y.; Yue, W. *Appl. Catal., A* **1998**, *169*, 127.

- (14) Peeters, M. P.; Busio, M.; Leijten, P. *Appl. Catal., A* **1994**, *118*, 51.
- (15) Wang, F.; Yang, G.; Zhang, W.; Wu, W.; Xu, J. *Chem. Commun.* **2003**, 1172.
- (16) Wang, F.; Yang, G.; Zhang, W.; Wu, W.; Xu, J. *Adv. Synth. Catal.* **2004**, *346*, 633.
- (17) Garade, A. C.; Bharadwaj, M.; Bhagwat, S. V.; Athawale, A.; Rode, C. V. *Catal. Commun.* **2009**, *10*, 485.
- (18) Kshirsagar, V. S.; Vijayanand, S.; Potdar, H. S.; Joy, P. A.; Patil, K. R.; Rode, C. V. *Chem. Lett.* **2008**, *37*, 310.
- (19) Stobbe, E. R.; Boer, B. A.; Geus, J. W. *Catal. Today* **1999**, *47*, 161.
- (20) Yamashita, T.; Vannice, A. J. *Catal.* **1996**, *163*, 158.
- (21) Edwards, H. W.; Harrison, R. M. *Environ. Sci. Technol.* **1979**, *13*, 673.
- (22) Yamashita, T.; Vannice, A. J. *Catal.* **1996**, *161*, 254.
- (23) Grootendorst, E.; Verbeek, Y.; Ponce, V. J. *Catal.* **1995**, *157*, 706.
- (24) An, G.; Yu, P.; Xiao, M.; Liu, Z.; Miao, Z.; Ding, K.; Mao, L. *Nanotechnology* **2008**, *19*, 275709.
- (25) Zhang, H.; Du, N.; Wu, P.; Chen, B.; Yang, D. *Nanotechnology* **2008**, *19*, 315604.
- (26) Yu, T.; Moon, J.; Park, J.; Park, Y. I.; Na, H. B.; Kim, B. H.; Song, I. C.; Moon, W. K.; Hyeon, T. *Chem. Mater.* **2009**, *21*, 2272.
- (27) Mukherjee, G. D.; Vaidya, S. N.; Karunakaran, C. *Phase Transitions* **2002**, *75*, 349.
- (28) Liu, Y.; Liu, Z.; Wang, G. *Appl. Phys. A* **2003**, *76*, 1117.
- (29) Antunes, E. F.; Lobo, A. O.; Corat, E. J.; Trava-Airoldi, V. J.; Martin, A. A.; Verissimo, C. *Carbon* **2006**, *44*, 2202.
- (30) Muduli, S.; Lee, W.; Dhas, V.; Mujawar, S.; Dubey, M.; Vijayamohan, K.; Han, S. H.; Ogale, S. *ACS Appl. Mater. Interfaces* **2009**, *1*, 2030.
- (31) Lee, G. W.; Kim, J.; Yoon, J.; Bae, J. S.; Shin, B. C.; Kim, I. S.; Oh, W.; Ree, M. *Thin Solid Films* **2008**, *516*, 5781.
- (32) Ramana, G. V.; Padya, B.; Kumar, R. N.; Prabhakar, K. V.; Jain, P. K. *Indian J. Eng. Mater. S.* **2010**, *17*, 331.
- (33) Lee, S. W.; Kim, B. S.; Chen, S.; Horn, Y. S.; Hammond, P. T. *J. Am. Chem. Soc.* **2009**, *131*, 671.
- (34) Apte, S. K.; Naik, S. D.; Sonawane, R. S.; Kale, B. B.; Pavaskar, N.; Mandale, A. B.; Das, B. K. *Mater. Res. Bull.* **2006**, *41*, 647.
- (35) Jiao, F.; Harrison, A.; Bruce, P. G. *Angew. Chem.* **2007**, *119*, 4020.
- (36) Audi, A. A.; Sherwood, P. M. A. *Surf. Interface Anal.* **2002**, *33*, 274.
- (37) Xie, X.; Li, Y.; Liu, Z. Q.; Haruta, M.; Shen, W. *Nature* **2009**, *458*, 746.
- (38) Hu, L.; Peng, Q.; Li, Y. *J. Am. Chem. Soc.* **2008**, *130*, 16136.
- (39) Bielanski, A.; Haber, J. *Catal. Rev.—Sci. Eng.* **1979**, *19*, 1.
- (40) Makwana, V. D.; Son, Y. C.; Howell, A. R.; Suib, S. L. *J. Catal.* **2002**, *210*, 46.
- (41) Wang, F.; Xu, J.; Liao, S. *Chem. Commun.* **2002**, 626.
- (42) Sokolovskii, V. D. *Catal. Rev.—Sci. Eng.* **1990**, *32*, 1.
- (43) Dadyburjor, D. B.; Jewur, S. S.; Ruckenstein, E. *Catal. Rev.—Sci. Eng.* **1979**, *19*, 293.
- (44) Palaniselvam, T.; Kannan, R.; Kurungot, S. *Chem. Commun.* **2011**, *47*, 2910.